

A Tight Grid-Forming Control Framework for Grid-connected Inverters under Large Grid Frequency Drops with Wide Range of SCR and X/R

Xitong Niu, *Student Member, IEEE*, Yue Qu, *Student Member, IEEE*, Pengfeng Lin, *Member, IEEE*, Chenggang Cui, *Member, IEEE*, Mrutyunjaya Sahani, *Senior Member, IEEE*, Chuanlin Zhang, *Senior Member, IEEE*, Sanjib Kumar Panda, *Fellow, IEEE*

Abstract—The high penetration of renewable energy sources in future power grids presents stability challenges for grid-connected inverters, particularly during large frequency drops under a wide range of short-circuit ratio (SCR) and X/R conditions. To address these challenges, especially for applications requiring firm power delivery such as utility-scale renewable plants under power purchase agreements, this paper proposes a tight grid-forming (TGFN) control framework. The primary objective of TGFN is to ensure precise and robust tracking of active power references, shifting the focus from passive frequency support to active and reliable power injection during grid disturbances. The proposed framework employs a grid voltage state observer to achieve real-time, high-fidelity estimation of the grid voltage's phase and frequency across diverse line impedance conditions. By integrating this real-time grid information into the controller, the inverter dynamically compensates for grid phase variations. This ensures a stable power angle, enabling the inverter to tightly track its power command and thereby preventing the overcurrent and oscillatory instabilities common during large frequency drops. The effectiveness of the proposed TGFN strategy is validated through comprehensive simulations and physical experiments under various grid conditions, demonstrating superior power tracking performance and stability.

Index Terms—tight grid-forming control, large grid frequency drops, disturbance observer, grid-connected inverters.

I. INTRODUCTION

THE increasing penetration of renewable energy sources (RESs) and power electronics (PEs) in future grids is leading to a continuous decline in grid inertia [1]–[3]. Currently, most grid-connected inverters (GCIs) deployed in power grids use grid-following (GFL) controls. This fact means GCIs inject currents to the grid, following the angle of grid voltage via phase-locked loops (PLLs), such that inverters can deliver either active or reactive power to the grid as per the discretion of system operators [4]. However, the application of GFL

This work was supported by the National Natural Science Foundation of China under Grant 62233006, and in part by the China Scholarship Council (CSC) under Grant 202411200003 and 202008310205. (*Corresponding author: Chuanlin Zhang*)

X. Niu, C. Cui and C. Zhang are with the Intelligent Autonomous Systems Laboratory, Shanghai University of Electric Power, Shanghai 200090, China (e-mail: xitongniu@mail.shiep.edu.cn; cgcui@shiep.edu.cn; clzhang@shiep.edu.cn).

Y. Qu is with the School of Electrical Engineering and Computer Science, the University of Queensland, Australia (e-mail: yue.qu@uq.edu.au).

P. Lin is with the School of Electrical Engineering, Shanghai Jiao Tong University, Shanghai, China (e-mail: pengfeng.lin@sjtu.edu.cn).

M. Sahani and S. K. Panda are with the Department of Electrical and Computer Engineering, National University of Singapore, Singapore (e-mail: mrutyunjayawahani@nus.edu.sg; eleskp@nus.edu.sg).

controls requires that the power system can maintain stability on its own. Therefore, grid-forming (GFM) controls have become increasingly popular in both industry and academia as they can enhance grid reliability and stability by simulating the behavior of a synchronous generator [5].

In spite of the advantages brought by GFM-based GCIs, their overcurrent capability is generally limited to approximately three times the rated current, which is significantly lower than that of physical synchronous generators, typically capable of withstanding 6 to 8 times the rated current [6]. In the case of unexpected events such as grid faults, significant load variations, or renewable power fluctuations, power systems may experience large frequency drops [7]. During such events, if the recovery process fails, GCIs may lose synchronization with the grid, potentially leading to overcurrent and oscillation issues [8]. Consequently, GCIs are likely to disconnect from the system, further aggravating power imbalances and frequency drops. Notably, large-scale power outages in the United Kingdom (2019) and Spain (2025) were linked to cascading shutdowns of RESs, possibly triggered by frequency deviations [9], [10]. Hence, ensuring both power injection stability and robust overcurrent protection is critical for GCIs under large grid frequency drops.

To protect grid-connected inverters (GCIs) from overcurrent damage, direct manipulation of the current reference or switch signals enables rapid and precise suppression. Current-reference saturation can be achieved using RMS [11], elliptical [12], or resonant-integrator [13] trackers to minimize distortion while preserving or prioritizing the current angle. Switch-level limiting instantly blocks PWM via hysteresis, achieving sub-cycle response [14]. In [15], the current-limiting challenge under a wide range of short-circuit ratios (SCRs) during voltage sags is investigated. Moreover, a composite power-frequency synchronization loop is proposed in [8] to address large frequency drops under high SCR conditions. However, the above-mentioned GCIs may operate in current-controlled mode during current-limiting operation, which can destabilize the system. Therefore, indirect current-limiting methods are adopted, such as power set-point modulation, which rescales power targets according to voltage drop [16]; virtual impedance, which subtracts a current-dependent voltage drop [17]; and switching to hysteresis control [18]. Nevertheless, these voltage-controlled methods may not be applicable across the wide range of SCR conditions expected in future power grids.

TABLE I
COMPARISONS OF PROPOSED METHOD AND RELATED METHODS FOR GRID-CONNECTED INVERTERS

References	Voltage Source Behavior	SCR	Large Frequency Drop	X/R
[11]–[14]	×	×	×	×
[15]		✓	✓	
[8]	✓	×	×	✓
[16]–[18]		✓	✓	
[19]–[21]	✓	✓	✓	✓
[22]		✓	✓	
[23], [24]	✓	✓	✓	✓
Proposed		✓	✓	

To better adapt to complex power systems, several methods have been proposed to enhance GCI performance across a wide range of SCRs. These include hybrid GFL-GFM controls [19], power self-synchronization strategies [20], and active admittance control [21]. However, these approaches mainly address small-signal stability, while GCI performance during large frequency drops remains less attended. While a power-angle-based strategy was proposed in [22] to achieve synchronization with current limiting, the broader challenges under varying grid conditions are not fully resolved.

It is worth noting that most of the aforementioned studies assume an inductive grid impedance, which is generally valid for high- or medium-voltage transmission systems [25]. However, in low-voltage grids, the X/R ratio is typically lower, which causes stronger coupling between active and reactive power [26]. Moreover, the power control behavior of GCIs can vary significantly under different combinations of SCR and X/R ratios [27], [28]. Although some work has focused on the adaptability across different X/R scenarios [23], [24], the stability as well as the overcurrent issue of GCIs under large frequency drops across a wide range of both SCR and X/R ratios is still rarely investigated.

GFM inverters should maintain a certain degree of voltage support capability even in current-limiting mode [29]. This requires two key abilities: 1) providing additional current output to support the grid during large frequency drops; 2) preserving stable voltage-source characteristics. Conventional strategies mitigate large frequency drops by passively limiting current [8] or voltage angle [22], and subsequently enhancing GFM capability [30]. However, in this way, grid dynamics still unpredictably influence the timing and magnitude of power delivery. This leads to the stability in current-limiting mode depending primarily on grid-side phase jumps rather than GCI's behavior. Motivated by modern renewable plant requirements—particularly solar farms and battery energy storage systems under strict Power Purchase Agreements (PPAs)—this paper re-examines the issue from a different perspective and reformulates the control strategy. By first ensuring stability and precise power tracking, the identified grid frequency enables active and accurate power support via the conventional $P-f$ characteristic—thereby achieving both required capabilities. Specifically, maintaining GFM capability under current-limiting conditions can be formulated as the problem of ensuring power tracking and stability at a power target corresponding to the maximum current.

Since a larger critical clearing angle (CCA) enhances system

stability during frequency drops [31], maintaining a constant power angle in GFM inverters under large frequency drops ensures that the CCA remains unchanged—thereby guaranteeing system stability. Consequently, the accurate real-time acquisition of grid voltage angle and frequency emerges as the pivotal challenge. This raises the question: how to reliably acquire and utilize this information over a wide range of SCR and X/R? While traditional PLLs can track the grid voltage angle, they exhibit stability issues in weak grids. In contrast, disturbance observer-based methods—successfully applied to load estimation in AC/DC microgrids [32]–[35]—provide faster, more robust model-based estimation of grid voltage angle disturbances. Requiring only knowledge of line impedance, this approach significantly enhances stability in complex grid conditions.

Motivated by the potential of observer-based estimation, this paper proposes a tight grid-forming (TGFM) control framework that ensures precise power tracking during severe grid disturbances. The core mechanism integrates a grid voltage state observer into the GFM control loop to sense and actively compensate for dynamic grid phase variations, thereby stabilizing the power angle and preventing instability. The main contributions are:

- 1) **Enhanced Stability while Retaining GFM Characteristics:** Real-time phase compensation during large frequency drops, preserving the inherent voltage-source characteristic of GFM control to prevent instability and disconnection.
- 2) **A New Control Paradigm for Grid Support:** Transition from passive frequency response to active, dispatchable power control, enabling the GCI to meet contractual obligations (e.g., PPAs) and support the grid controllably under diverse conditions.
- 3) **Guaranteed Large-Signal Stability:** Lyapunov-based proof of large-signal stability, ensuring rapid convergence of observer estimation error under large frequency drops and wide variations in SCR and X/R.

The subsequent sections are organized as follows: Section II carries out the problem formulation. Section III describes the proposed control strategy. Simulations and the experimental validations are carried out in Section IV. Conclusions are given in the last section.

II. PROBLEM FORMULATION

The topology of the investigated system is shown in Fig. 1, including a three-phase inverter linked to the point of common coupling (PCC), a line impedance, and an AC grid. In this model, L_f , R_f , and C_f are the filter inductance, resistance, and capacitance, respectively, while L_g and R_g represent the line inductance and resistance. Voltage and current sensors are placed at the PCC. The active power P and reactive power Q are calculated from the PCC voltage (u_{pa} , u_{pb} , u_{pc}) and the grid-side current (i_{ga} , i_{gb} , i_{gc}). P_r and Q_r are the active and reactive power references for the GFM controller.

A. Mathematical Model of the Investigated System

According to Kirchhoff's laws, the dynamics of the inverter's LCL filter are formulated as:

$$\begin{cases} L_f \dot{i}_{L_f \kappa} = u_{\kappa} - u_{p\kappa} - R_f i_{L_f \kappa}, \\ C_f \dot{u}_{p\kappa} = i_{L_f \kappa} - i_{g\kappa}, \end{cases} \quad (1)$$

where $\kappa = a, b, c$ denotes each phase, u_{κ} represents the inverter's output terminal voltage, $u_{p\kappa}$ is the PCC voltage, $i_{L_f \kappa}$ is the inductor current, and $i_{g\kappa}$ is the current injected into the grid from the PCC. The inverter bridge generates the voltage u_{κ} based on the reference signals provided by the GFM controller via space vector PWM.

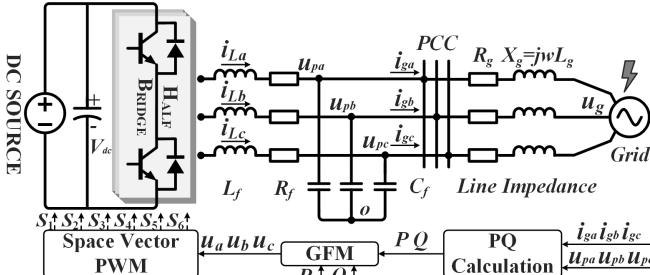


Fig. 1. Topology of the investigated system.

The relationship between the PCC voltage and the grid voltage through the line impedance is given by:

$$L_g \dot{i}_{g\kappa} + R_g i_{g\kappa} = u_{p\kappa} - u_{g\kappa}, \quad (2)$$

where $u_{g\kappa}$ is the voltage of the AC grid. The active and reactive power flowing from the PCC to the grid can be calculated as:

$$\begin{cases} P = \frac{3U_p}{R_g^2 + X_g^2} [R_g(U_p - U_g \cos \delta) + X_g U_g \sin \delta], \\ Q = \frac{3U_p}{R_g^2 + X_g^2} [X_g(U_p - U_g \cos \delta) - R_g U_g \sin \delta], \end{cases} \quad (3)$$

where U_p and U_g are the voltage amplitudes of $u_{p\kappa}$ and $u_{g\kappa}$, respectively, and $X_g = \omega L_g$ is the grid reactance. The power angle $\delta = \phi_p - \phi_g$ is defined as the phase difference between the PCC voltage phasor (with angle ϕ_p) and the grid voltage phasor (with angle ϕ_g), relative to a common stationary reference frame.

Remark 1: Although the proposed control strategy utilizes grid impedance parameters for the grid voltage observer, accurate grid impedance acquisition is a well-established field (e.g., via signal injection [23]). Specifically, an event-driven online grid impedance estimation algorithm is embedded in the adaptive VSG control loop. It injects a 75 Hz single-frequency perturbation using only PCC voltage and current measurements, requiring no additional hardware and minimally affecting power quality. The estimation error remains within 1% in both strong and weak grid conditions.

B. Mathematical Model of the VSG Control System

As depicted in Fig. 2, a conventional Virtual Synchronous Generator (VSG) control structure is considered.

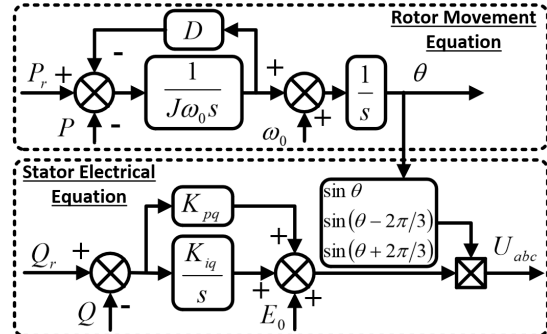


Fig. 2. Control diagram of the VSG strategy.

For stability analysis and parameter design, the system can be linearized around a steady-state operating point. The resulting small-signal model, which relates the active power reference P_r to the output power P , is given by [23]:

$$\frac{\Delta P}{\Delta P_r} = \frac{G_p(s)(K_{11} + MG_q(s))}{1 + K_{11}G_p(s) + K_{22}G_q(s) + MG_p(s)G_q(s)}, \quad (4)$$

where $G_p(s) = \frac{1}{s(J\omega_0 s + D)}$ represents the dynamics of the VSG's swing equation, incorporating virtual inertia J and damping D . The term $G_q(s)$ is the transfer function for the reactive power PI controller. The coefficients K_{11} , K_{12} , K_{21} , and K_{22} are linearization gains that are functions of the system's operating point (i.e., voltage amplitudes U_p , U_g and power angle δ) and the line impedance (R_g , X_g). As their full expressions are extensive, they are omitted here for brevity.

Remark 2: To ensure a stable and well-damped performance, the VSG parameters are typically tuned to achieve a desired second-order dynamic response, as described in III. A in [23]. However, the calculation requires assuming a fixed grid angle, typically $\phi_g = 0$. This assumption, while valid in steady-state, becomes incorrect during large grid frequency drops. The resulting parameter mismatch can compromise controller performance and lead to instability—the very problem this paper addresses.

C. Impact of Grid Frequency Drops on Power Angle Stability

From a GFM inverter's perspective, a large grid frequency drop manifests as a continuous negative deviation of the grid's phase angle ϕ_g . As illustrated in Fig. 3, this forces the system's operating point to move along its power-angle characteristic, for instance from state "(1)" towards "(10)".

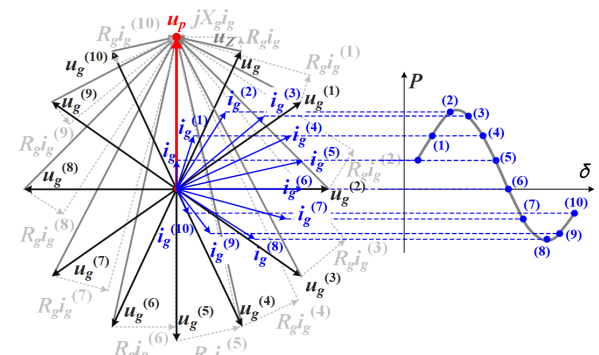


Fig. 3. Direct impact of a growing power angle on grid current and power.

The corresponding phasor diagrams, showing vectors among u_p , u_g and u_Z ($u_Z = R_g i_g + j X_g i_g$), reveal a continuous increase in i_g , pushing the inverter towards its operational limits. If this deviation persists, the system's power and current may begin to oscillate.

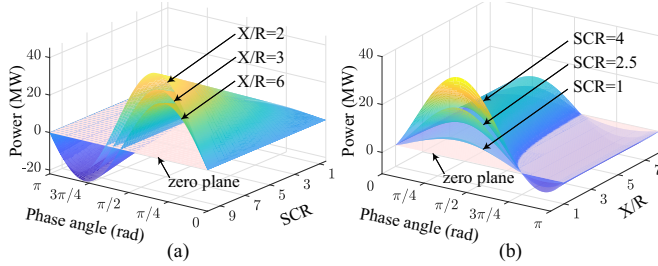


Fig. 4. Dependence of the power-angle relationship on SCR and X/R.

However, the severity of this effect and the stability landscape itself are not fixed, but are critically dependent on the grid's specific impedance, characterized by its SCR and X/R. Considering $Q_r = 0$, the relationship among u_p , δ and grid parameters can be expressed as $u_p = u_g(R_g/X_g \sin \delta + \cos \delta)$ based on (3). As demonstrated in Fig. 4, the grid parameters fundamentally reshape the $P - \delta$ relationship: 1) For a given X/R ratio, a lower SCR reduces the maximum power transfer capability, shrinking the stability margin. 2) For a given SCR, a higher X/R ratio can narrow the viable power angle range.

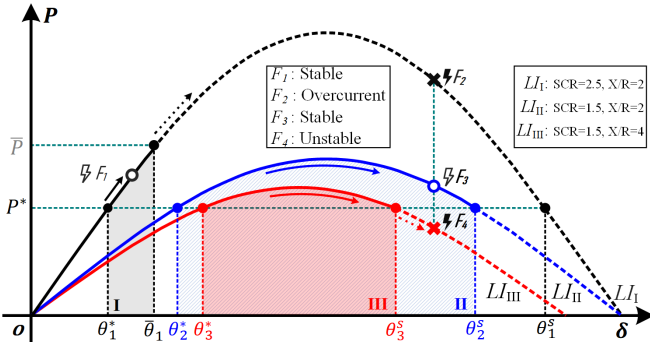


Fig. 5. Typical $P - \delta$ curves illustrating different stability outcomes for various line impedances.

Subsequently, different potential outcomes of a disturbance are analyzed for three typical line impedances— LI_1 (SCR=2.5, X/R=2), LI_{II} (SCR=1.5, X/R=2), and LI_{III} (SCR=1.5, X/R=4)—as shown in Fig. 5. The power angle corresponding to the target power P^* is denoted as θ^* , and the CCAs are denoted as θ_i^s for $i = 1, 2, 3$. The power angle at the maximum allowable power \bar{P} for LI_1 is θ_1 . The unsaturated curve (solid black) represents the $P-\delta$ characteristic when the current limiter is inactive. The dashed black curve represents the $P-\delta$ characteristic for LI_1 without current saturation. The pale black, pale blue, and pale red areas (I, II, and III, respectively) represent the stable operating regions for LI_1 , LI_{II} , and LI_{III} under the disturbance. The solid blue and red curves represent the $P-\delta$ characteristics of the stable systems with LI_{II} and LI_{III} , respectively. The dashed blue and red curves represent the $P-\delta$ characteristics of the unstable systems with LI_{II} and LI_{III} , respectively.

Remark 3: For a current-limited GFM inverter, the CCA is determined as the intersection point between the P^* and the

$P-\delta$ curve under current limiting, as derived in [36].

Depending on the disturbance severity and line impedance, three outcomes are possible:

- **Stable Recovery:** For a small disturbance, the power angle deviates from θ^* but remains within a recoverable region, allowing the system to return to a stable equilibrium (e.g., F_1).
- **Compromised Operation via Current Limiting:** If the angle deviation grows until the current reaches the protection threshold (e.g., F_2 , where the angle exceeds θ_1), current-limiting controls are triggered. The inverter then operates as a constant-current source, losing its voltage-source characteristic and active regulation capability.
- **Transient Instability:** If the disturbance is sufficiently severe, the power angle may exceed the stability boundary (e.g., θ_3^s in case F_4), leading to a complete loss of synchronism (pole slipping). Crucially, the outcome is impedance-dependent: for the same angle deviation in case F_3 , the system with LI_{II} may recover, while the system with LI_1 may have already entered current limiting (as in F_2).

To sum up, an inverter's response to a frequency drop is hard to predict; it depends on both the disturbance's severity and the specific grid impedance. Generally speaking, a larger CCA of the designed system is the target. However, the ultimate failure can be a forced transition into a compromised, passive current-limiting state or a complete loss of synchronism. This unpredictable and passive nature of the response underscores the critical need for real-time grid phase information, which would enable a proactive and intelligent control strategy.

III. PROPOSE TIGHT GRID FORMING CONTROL FOR GCIs

To address the stability challenges outlined in Section II, this paper proposes a Tight Grid-Forming (TGF) control framework. The core principle is to shift from a passive response to an active, adaptive strategy by leveraging real-time grid information. This is achieved by integrating a grid voltage observer into the GFM control loop to enable precise power tracking while retaining robust voltage-source characteristics.

A. Grid Voltage Observer

To obtain the dynamic state of the grid voltage, a disturbance observer-based approach is adopted, inspired by [37]. The uncertain grid voltage $u_{g\kappa}$ is estimated by the following grid voltage observer:

$$\begin{cases} \hat{u}_{g\kappa} = \lambda(p_\kappa - i_{g\kappa}), \\ L_g \frac{dp_\kappa}{dt} = u_{p\kappa} - \hat{u}_{g\kappa} - R_g i_{g\kappa}, \end{cases} \quad (5)$$

where p_κ are the auxiliary state variables of the observer and λ is a positive constant, denoted as the observer gain, which determines the estimation bandwidth. The structure of the observer is shown in Fig. 6.

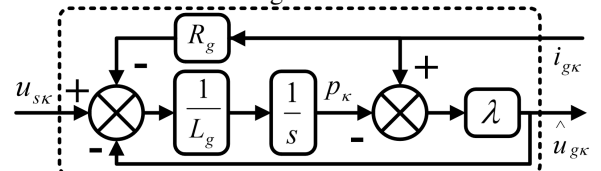


Fig. 6. Estimation framework of the grid voltage.

B. Proposed TGFM Framework

The proposed TGFM control framework, depicted in Fig. 7, integrates the observer's output into a conventional VSG structure. The key mechanism is the feed-forward compensation of the grid phase angle.

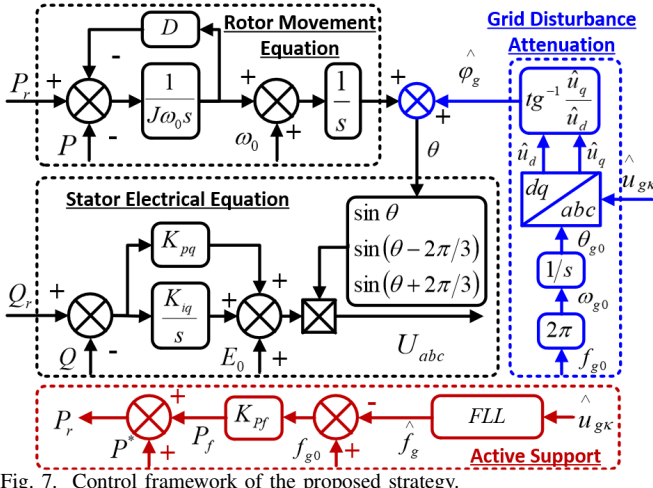


Fig. 7. Control framework of the proposed strategy.

The “Grid Disturbance Attenuation” block uses pre-synchronization values f_{g0} and ϕ_{g0} for the Park transform. When $P^* = 0$, the rotor movement equation output equals ϕ_{g0} . Frequency drops induce dynamics in \hat{u}_d and \hat{u}_q , yielding grid phase deviation $\Delta\phi_g = (\hat{u}_q, \hat{u}_d)$.

The estimated voltage $\hat{u}_{g\kappa}$ also feeds a frequency-locked loop (FLL) to obtain \hat{f}_g . Using $P-f$ droop, active support power $P_f = K_{Pf}(f_{g0} - \hat{f}_g)$ is generated ($K_{Pf} > 0$). The total reference becomes $P_r = P^* + P_f$. Injecting $\Delta\phi_g$ into the VSG angle compensates phase shifts in real-time while dispatching P_f during frequency events—unifying disturbance attenuation and active grid support.

C. Stability Analysis and Mechanism

The stability of the proposed TGFM framework hinges on a crucial insight: the feed-forward compensation transforms the large, potentially destabilizing grid phase deviation into a small, manageable disturbance for the inverter. From the VSG's perspective, the only remaining power angle disturbance it must handle is the observer's small, bounded estimation error. The stability can be formally analyzed as follows.

1) *Bounded Observer Error:* To demonstrate that the estimation error is bounded, the unknown voltage, denoted by $u_{g\kappa}$, can be modeled as:

$$u_{g\kappa}(t) = U_{g0} \sin(\omega_g t + \phi_{g0}), \quad (6)$$

where $\omega_g = 2\pi f_g = 2\pi(f_{g0} + \Delta f_g)$ is the angular frequency, Δf_g is the frequency offset, $\phi_{g0} = 0$ is the initial phase.

Then the derivative of $u_{g\kappa}$ can be expressed as

$$\dot{u}_{g\kappa} = U_{g0}\omega_g \cos(\omega_g t + \phi_{g0}). \quad (7)$$

Define the observation error as

$$e_u = u_{g\kappa} - \hat{u}_{g\kappa}. \quad (8)$$

Subsequently, by taking derivatives of (8) and based on (5), the error dynamics can be derived from the system and observer equations

$$\begin{aligned} \dot{e}_u &= \dot{u}_{g\kappa} - \lambda(\dot{p}_\kappa - \dot{i}_{g\kappa}) \\ &= \dot{u}_{g\kappa} - \lambda(u_{p\kappa} - \hat{u}_{g\kappa} - R_g i_{g\kappa} - L_g \dot{i}_{g\kappa})/L_g. \end{aligned} \quad (9)$$

Then, the error dynamics can be further derived by substituting (2) into (9)

$$\dot{e}_u = \dot{u}_{g\kappa} - \lambda(-\hat{u}_{g\kappa} + u_{g\kappa})/L_g = \dot{u}_{g\kappa} - \lambda e_u/L_g. \quad (10)$$

Choose a Lyapunov function as $V = \frac{1}{2}e_u^2$, then the derivative of V can be written as

$$\dot{V} = e_u \dot{e}_u = e_u (\dot{u}_{g\kappa} - \lambda e_u/L_g). \quad (11)$$

Since $|\dot{u}_{g\kappa}| \leq U_{g0}\omega_g$, one can derive that

$$\dot{V} \leq |e_u|U_{g0}\omega_g - \lambda e_u^2/L_g. \quad (12)$$

Since $e_u \neq 0$, hence $\dot{V} < 0$ is satisfied when the following relation exists

$$|e_u| > U_{g0}\omega_g L_g / \lambda. \quad (13)$$

Thus, the observation error e_u is gradually bounded and converges to the region $U_{g0}\omega_g L_g / \lambda$.

The exponential term decays to zero when $t \rightarrow \infty$ and yields the steady-state error

$$e_u(\infty) = \int_0^\infty e^{-\frac{\lambda}{L_g}\tau} U_{g0}\omega \cos(\omega\tau + \phi_{g0}) d\tau. \quad (14)$$

Using the integral formula:

$$\int_0^\infty e^{-a\tau} \cos(b\tau + c)d\tau = \frac{a \cos c - b \sin c}{a^2 + b^2}, \quad (15)$$

where $a = \lambda/L_g$, $b = \omega$, $c = \phi_{g0} = 0$. Hence one can get:

$$e_u(\infty) = \frac{U_{g0}\omega\lambda/L_g}{(\lambda/L_g)^2 + \omega^2}. \quad (16)$$

The phase deviation $\Delta\phi$ is calculated from the frequency response of the observer's transfer function. The observer's transfer function is defined as follows:

$$\hat{U}_{g\kappa}(s) = \frac{\lambda}{s + \lambda/L_g} U_{g\kappa}(s). \quad (17)$$

In the frequency domain, let $s = j\omega_g$, then the phase deviation $\Delta\phi$ can be expressed as the phase of the transfer function:

$$\Delta\phi = -\arctan(\omega_g L_g / \lambda). \quad (18)$$

Based on (18), the relationship among L_g , λ , $\Delta\phi$, and frequency is shown in Fig. 8.

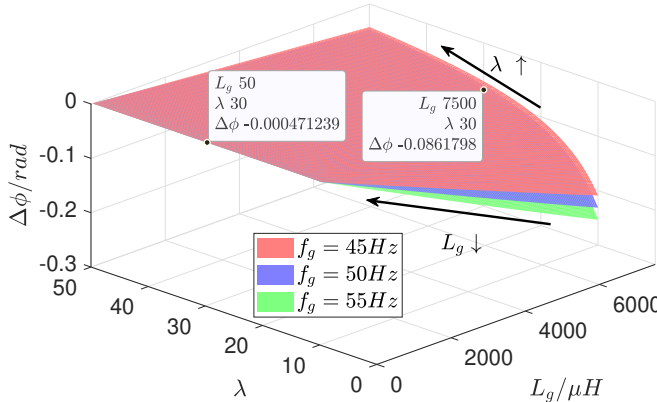


Fig. 8. 3D mesh surface of L_g , λ , and $\Delta\phi$ versus frequency.

Fig. 8 shows that $\Delta\phi$ decreases with reducing L_g and increasing λ , while remaining nearly frequency-independent. Thus, the observer gain λ should be selected to satisfy:

- 1) $\Delta\phi < \theta^s - \theta^*$, ensuring the operating point stays below the CCA during frequency disturbances;
- 2) $\Delta\phi < \bar{\theta} - \theta^*$, limiting power angle excursion to $\delta = \bar{\theta} + \Delta\phi$ under current saturation ($\delta = \bar{\theta}$), thereby preserving voltage-source behavior and preventing disconnection.

where θ^* is the power angle at target power P^* , $\bar{\theta}$ is the power angle at maximum allowable power \bar{P} under current limiting, and θ^s is the CCA marking the onset of instability.

2) *Overall Stability Mechanism:* Feed-forward compensation reduces the power-angle deviation seen by the VSG to the bounded observer error $\Delta\phi$, rather than the uncontrolled grid phase jump. Thus, if $\Delta\phi$ stays below the CCA margin ($\theta^s - \theta^*$), the inverter remains stable. Hence the Lyapunov analysis proves system stability. Physically, with the observer tracking grid voltage phase, the GFM handles only the minor observation error—a smooth, bounded disturbance—ensuring both stability and tracking accuracy under severe grid events.

D. Comparison with Conventional GFM and Other Controls

The proposed TGFN outperforms conventional GFM and alternative strategies in terms of control objectives, response, stability, and overcurrent management.

1) *Control Objectives:* Conventional GFM emulates synchronous machines via PCC voltage regulation and passive grid support. TGFN, however, prioritizes accurate power tracking to enable dispatchable injection, transforming the GCI into a reliable power source.

2) *Response and Stability:* During frequency drops, conventional GFM depends on passive power-angle growth, risking instability. TGFN actively estimates grid phase in real time, compensates output voltage, and aligns power angle with reference—preventing overcurrent and oscillations.

3) *Overcurrent Capability:* Conventional GFM suffers passive, uncontrollable overcurrent that exhausts margins. Post-limiting, power drops with rising angle, weakening frequency support; large drops may exceed CCA, causing instability. TGFN actively schedules overcurrent via real-time frequency estimation and power tracking, preserving margins and support capability to enhance recovery and stability.

4) *Control Structure Analysis:* PLL-based methods rely on local voltage and may lose lock in weak/disturbed grids. TGFN integrates observed grid phase directly into conventional GFM output, converting severe frequency-drop events into manageable tracking-error problems while preserving GCI voltage-source behavior.

IV. SIMULATION AND QUANTITATIVE ANALYSIS

A. Simulation Verification

1) *Simulation Setup:* Simulations are conducted in MATLAB/SIMULINK, using the parameters provided in TABLE II. In the simulation, the grid frequency is subjected to a severe drop of 1.6 Hz at $t = 3$ s, which persists for 3 seconds.

TABLE II
SYSTEM PARAMETER CONFIGURATION

Parameter	Description	Value	Unit
U_{g0}	grid voltage (L-L)	690	V _{rms}
f_{g0}	nominal grid frequency	50	Hz
S_N	inverter rated power	5	MVA
v_{dc}	voltage of the dc side	3000	V
L_f	nominal filter inductance	95	μH
C_f	nominal filter capacitance	1	mF
R_f	nominal filter resistance	0.01	Ω
f_{sw}	inverter switching frequency	10	kHz
T_c	control period	100	μs
λ	observer gain	2	-
R_{g1}, L_{g1}	Case 1: SCR=8, X/R=7	1.68, 37.5	$m\Omega, \mu H$
R_{g2}, L_{g2}	Case 2: SCR=8, X/R=5	2.3, 37.1	$m\Omega, \mu H$
R_{g3}, L_{g3}	Case 3: SCR=1.5, X/R=7	8.9, 200	$m\Omega, \mu H$
R_{g4}, L_{g4}	Case 4: SCR=1.5, X/R=1	44.9, 142.8	$m\Omega, \mu H$

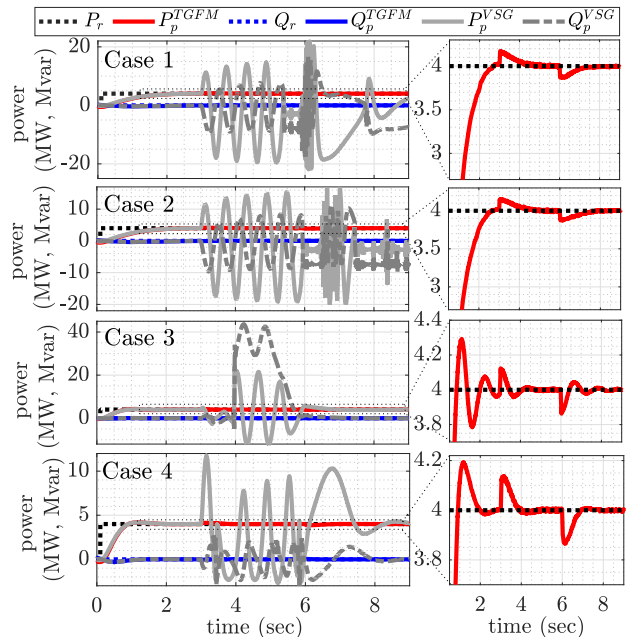


Fig. 9. Performance of the power with the VSG and the TGFN strategy.

2) *Performance Comparison under Large Frequency Drop:* As shown in Fig. 9, TGFN and conventional GFM (VSG) perform identically before the drop ($t = 3$ s). Post-drop, VSG exhibits severe power oscillations and power-angle divergence in all four cases (Fig. 11); parameter mismatch further drives instability (Fig. 12 (a)-(d)).

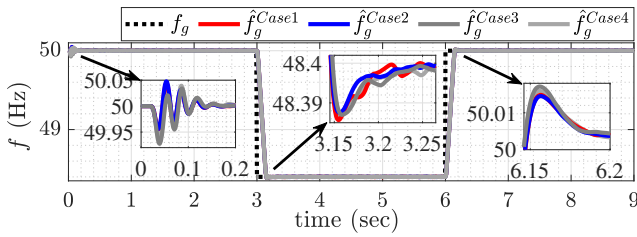


Fig. 10. Frequencies and estimations of grid voltage.

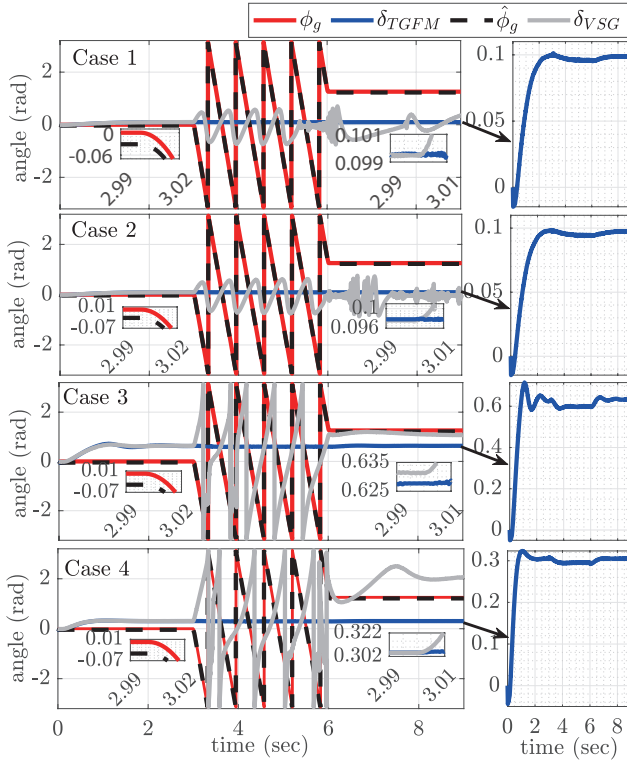


Fig. 11. Voltage power angle δ with the VSG and the TGFM strategy.

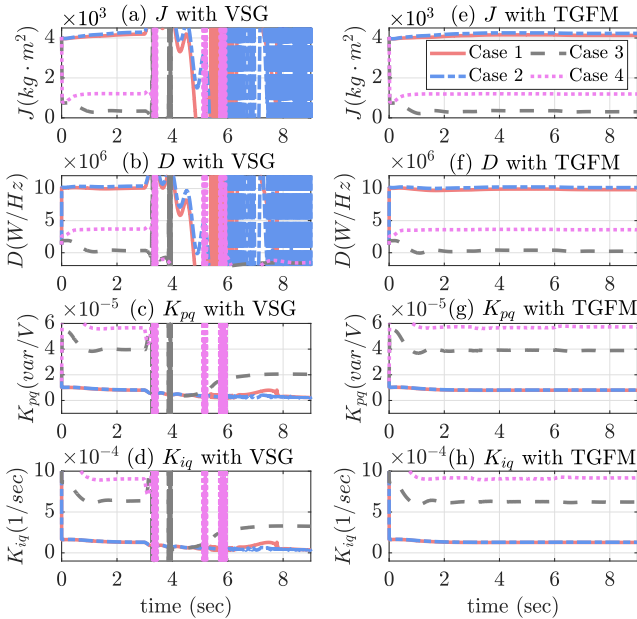


Fig. 12. Control parameter of the VSG and TGFM strategy.

In contrast, TGFM maintains stable operation. With a 4 MW reference, power fluctuations stay below 0.2 MW, tracking

remains accurate, and recovery completes within 1.5 s (Fig. 9). Transients show power rising during the drop and falling upon recovery. This stability stems from real-time grid frequency and phase estimation (Fig. 10). TGFM suppresses power-angle excursions to <0.02 rad across all cases (Fig. 11), eliminating the oscillations and divergence seen in VSG.

Furthermore, as shown in Fig. 12 (e)-(h), TGFM maintains consistent VSG parameters before and after the frequency drop. Analysis of the parameters demonstrates that the proposed method adapts to various line impedances. Moreover, the consistency of parameters during the frequency drop is reasonable, as these parameters are primarily influenced by impedance variations rather than grid voltage changes. Thus, combining TGFM's performance in power angle stability and parameter consistency, it is validated that the proposed method transforms the issue of significant frequency drops into a problem of power error regulation.

B. Quantitative Analysis

This section will provide a quantitative result of the four cases in TABLE II, analyzing why the oscillations and the overcurrent issue can be prevented. Firstly, the CCA can be determined through zero-pole analysis of (4) with different phase angles. Then, the observation errors of the grid voltage phase angle are calculated. With the observation errors within the CCA, the oscillations can be avoided. Furthermore, with the application of the power angle equation, the phase angle of the overcurrent point can also be calculated. Similarly, if only the observation errors are within these angles, the overcurrent can also be avoided.

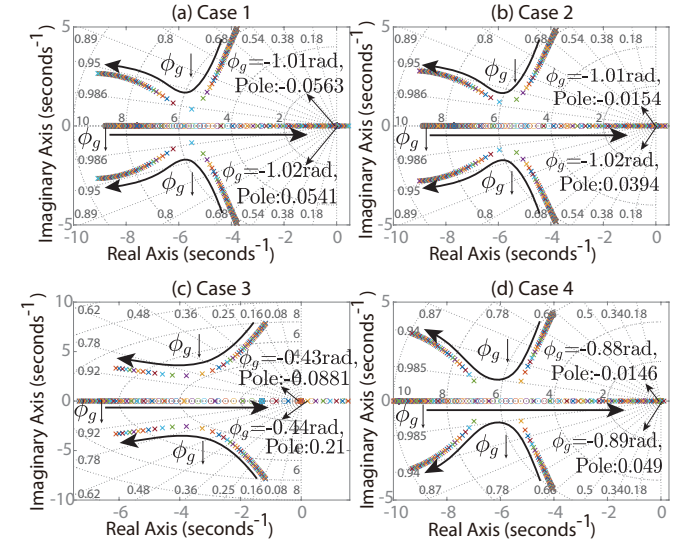


Fig. 13. Pole-Zero maps of (4) with four cases under grid phase angle drops.

1) **Acquisition of CCA:** As shown in Fig. 13, the closed-loop poles and zeros of (4) are plotted for phase angles from 0 to -1.1 rad across Cases 1–4. The pole trajectories show that decreasing grid phase shifts the dominant poles toward the right-half plane, indicating impending instability. The instability boundaries (i.e., the CCAs) are -1.01 , -1.01 , -0.43 , and -0.88 rad, respectively. This confirms that identical power targets yield different stability limits under varying line impedances.

2) *Observation Analysis:* The convergence speed is determined by the time constant $\tau = L_g/\lambda$. The observation time T is defined as the time required for the error to decay to ϵ of its initial value $T = -(L_g/\lambda) \ln(\epsilon)$. For $\epsilon = 1\%$, this becomes $T \approx 4.605L_g/\lambda$. The following parameters are used for quantitative analysis $\omega_g = 2\pi \times 48.4 \approx 304.11 \text{ rad/s}$, $\lambda = 2$. Then the steady-state error, convergence time constant, observation time and phase deviation for each case are calculated and summarized in TABLE III.

TABLE III
QUANTITATIVE RESULTS FOR OBSERVER PERFORMANCE

Parameter	Description	Unit	Case 1	Case 2	Case 3	Case 4
$ e_u(\infty) $	Steady-State Error	V	0.64	0.64	0.34	0.40
τ	Time Constant	μs	18.75	18.55	100	71.4
T	Observation Time	μs	86.34	85.42	460.5	328.7
$\Delta\phi_g$	Phase Deviation	rad	-0.01	-0.01	-0.03	-0.02

The observer design ensures stability and bounded observation error. The key results are: 1) Steady-state error is inversely proportional to λ . 2) Convergence speed and observation time depend on $\tau = L_g/\lambda$. 3) Phase deviation is small and can be further reduced by increasing λ .

3) *Analysis of Stability Mechanism:* The proposed method's stability is driven by the grid state observer's performance, which ensures small observation errors compared to the instability boundaries. By comparing the observation error with the theoretical CCA, it is evident that after incorporating the observed phase of the grid voltage into the output voltage of the conventional VSG controller, the power angle of the GCI is significantly smaller than the CCA. Consequently, the stability of the power angle during large-scale frequency drops is greatly enhanced.

4) *Analysis of Overcurrent Protection:* As derived in (3) and Table II, the theoretical power angles at target power are 0.1, 0.1, 0.64, and 0.3 rad for Cases 1–4, respectively. With observer error $\Delta\phi_g$, the proposed method shifts the current-limited angles to 0.11, 0.11, 0.67, and 0.32 rad (Fig. 14), increasing power to 4.48, 4.55, 4.22, and 4.10 MW. This slight power and angle boost preserves GFM voltage-source behavior under current saturation.

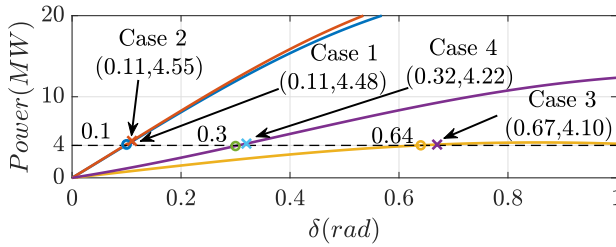


Fig. 14. Overcurrent analysis with $P - \delta$ under four cases.

V. EXPERIMENTAL RESULTS

To validate the effectiveness and priority of the proposed control strategy, a small-scale experimental platform, as shown in Fig. 15, has been constructed to perform several experiments. As shown in Fig. 15, the grid can be represented by the

three-phase resistive loads and a three-phase AC power source. The complex line impedance scenario can be modeled with real inductors and resistors. The three-phase inverter consists of inductors, capacitors and three SiC MOSFET half-bridge modules. The dc power is from a dc power source and a rectifier.

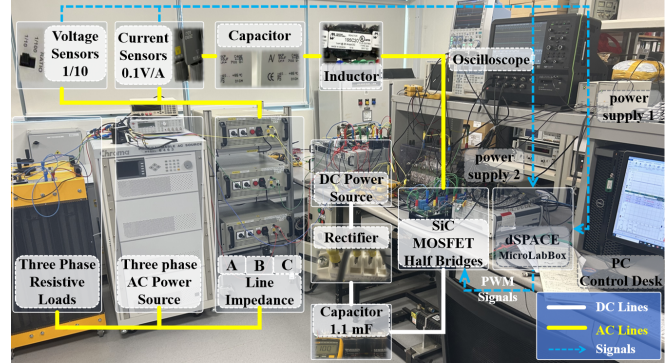


Fig. 15. Experimental Setup.

The signals of the current sensors, voltage sensors and MOSFET drive ports are connected to the dSPACE MicroLabBox. The voltages of phase A at the PCC and grid side, the phase A current flowing into the grid and the active power are displayed in oscilloscope.

A. Comparison Results

Due to the limited current and voltage of the devices in the laboratory, the grid voltage amplitude is intentionally reduced to create a wide range of SCR and X/R. The experimental setup parameters for comparison are listed in TABLE IV.

TABLE IV
EXPERIMENTAL SETUP PARAMETERS

Variables	Description	Value
V_{dc}	DC voltage	50 V
S	Rated capacity	70.7 VA
P	Rated active power	50 W
U_g	AC side voltage	10 V _{rms}
f_{g0}	Nominal Grid Frequency	50 Hz
L_f	one phase inductance	1.2767 mH
C_f	one phase capacitance	15.059 μF
R_f	one phase resistance	0.03 Ω
λ	observer gain	30

The line impedance cases under study as well as the corresponding SCR and X/R based on TABLE IV are all recorded in TABLE V. L_g and R_g in TABLE V are measured with a programmable LCR bridge.

TABLE V
FOUR CASES OF LINE IMPEDANCE

Case	X/R	SCR	L_g (mH)	R_g (Ω)
1	1.9	5.5	2.2	0.4
2	1.6	1.8	6.5	1.3
3	6.8	6.1	2.2	0.1
4	9.4	2.1	6.5	0.22

The experimental results are shown in two sets of figures. Figs. 16–19 present oscilloscope captures for the 4 cases, displaying PCC voltage u_{pa} , grid voltage u_{ga} , grid-injected current i_{ga} , and active power P_p over a 10 s window and two zoom windows of the 0.1 Hz and 2 Hz drop, respectively.

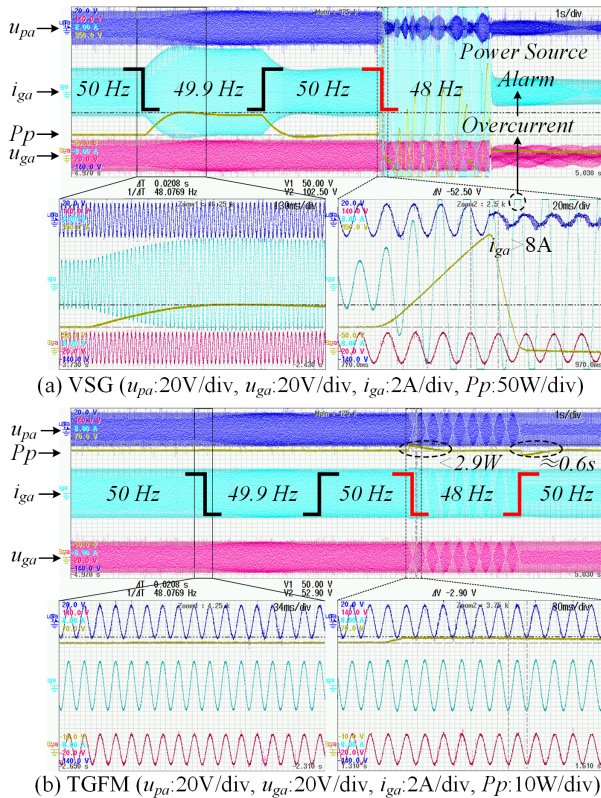


Fig. 16. Experimental waveforms of VSG and TGFM with Case 1.

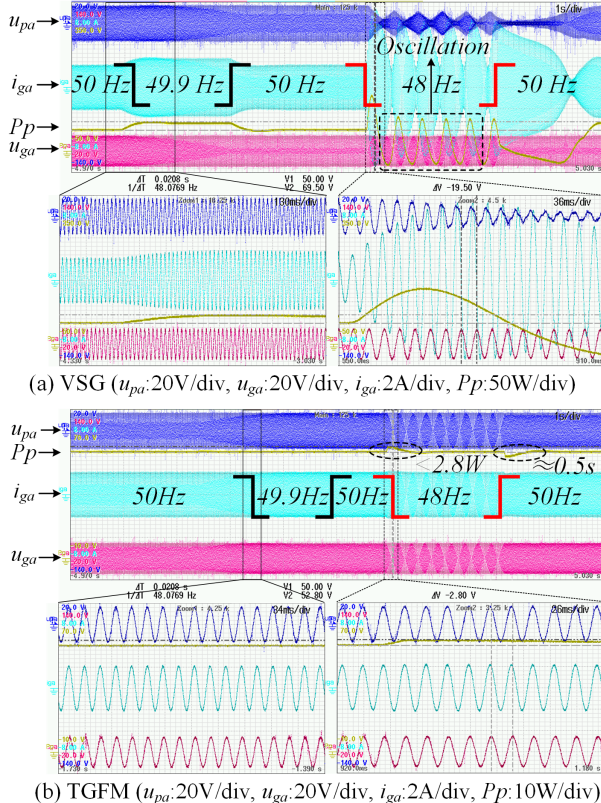


Fig. 17. Experimental waveforms of VSG and TGFM with Case 2.

Figs. 20-22 provide the relationship among active power of VSG (P_{VSG}), TGFM (P_{TGFM}) and target (P_r), reactive power of VSG (Q_{VSG}), TGFM (Q_{TGFM}) and target (Q_r), and grid frequency f_g across all four cases.

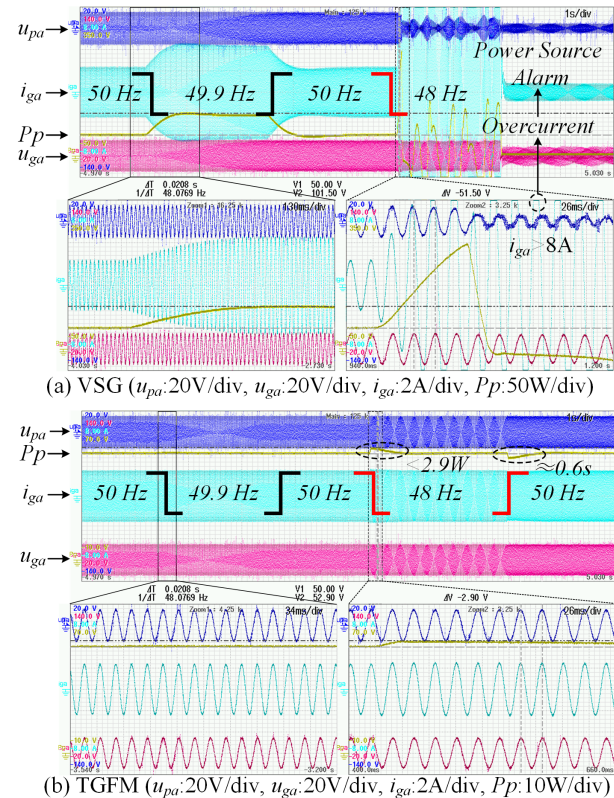


Fig. 18. Experimental waveforms of VSG and TGFM with Case 3.

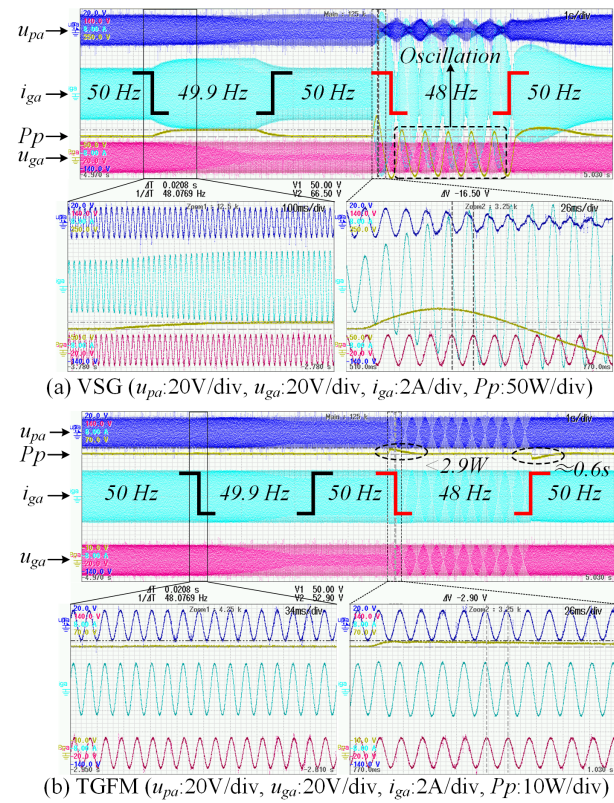


Fig. 19. Experimental waveforms of VSG and TGFM with Case 4.

1) *SCR Characteristic Analysis:* a. For 0.1 Hz drop, as depicted in Fig. 16 (a) and Fig. 17 (a), VSG injects 52.5 W and 19.5 W, respectively. And similarly in weak grid scenario, Fig. 18 (a) and Fig. 19 (a) show that VSG injects 51.5 W and

16.5 W, respectively. b. For 2 Hz drop, as depicted in Fig. 16 (a) (Case 1), P_{VSG} triggered the power source alarm due to the overcurrent protection (OCP). While in Fig. 17 (a) (Case 2), OCP are not triggered. And in weak grid scenario, OCP is triggered in Fig. 18 (a) (Case 3) and not in Fig. 19 (a) (Case 4). These phenomena demonstrate the description in Fig. 4 (b) that higher SCR at similar X/R ratio results in higher power.

2) *X/R Characteristic Analysis*: a. For 0.1 Hz drop, as depicted in Fig. 16 (a) and Fig. 18 (a), VSG injects 52.5 W and 51.5 W, respectively. And similarly in weak grid scenario, Fig. 17 (a) and Fig. 19 (a) show that VSG injects 19.5 W and 16.5 W, respectively. b. For 2 Hz drop, as depicted in Fig. 16 (a) and Fig. 18 (a), P_{VSG} surges to 266 W in 94 ms (Case 1) and 244 W in 98 ms (Case 3), respectively. And in weak grid scenario, Fig. 17 (a) and Fig. 19 (a) VSG exhibits a 0.5 s periodic oscillation: from -30 W to 75 W (Case 2) and -45 W to 60 W (Case 4). These phenomena demonstrate the illustration in Fig. 4 (a) that lower X/R ratios at similar SCR result in higher power/oscillation peaks.

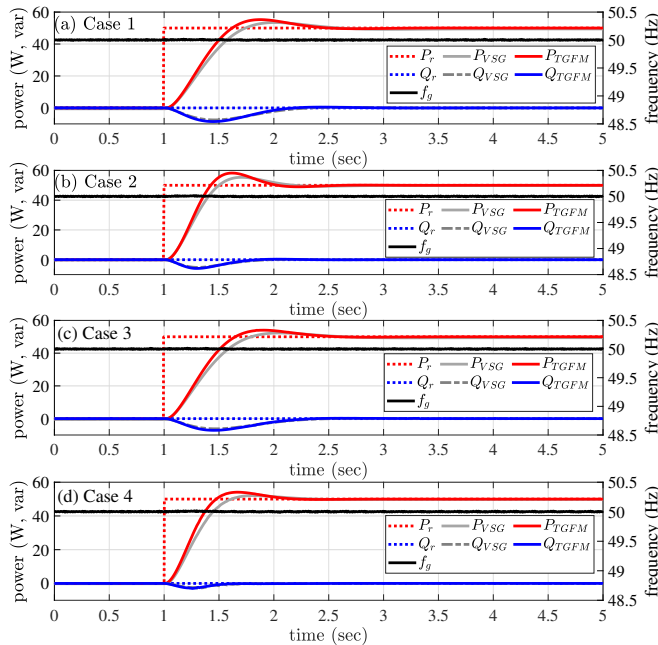


Fig. 20. Loading process of VSG and TGFM with different line impedance.

3) *Load Step Response*: In Fig. 20, both VSG and TGFM track the P_r within 1.5 s following a step change. The proposed TGFM achieves higher steady-state accuracy, with deviations below 0.005 W across all cases, whereas VSG exhibits case-dependent settling errors up to 0.55 W, 0.19 W, 0.54 W and 0.19 W, respectively.

4) *Small Frequency Drop ($\Delta f = 0.1$ Hz)*: In Fig. 21, VSG delivers inconsistent inertial support: 52.5 W, 19.5 W, 51.5 W and 16.5 W, respectively. This variation confirms that conventional GFM-based GCIs lack controllable power output. In contrast, TGFM maintains 0.13 W increase and recover to power target within 0.6 s in all cases.

5) *Large Frequency Drop ($\Delta f = 2$ Hz)*: In Fig. 22, VSG fails due to overcurrent (Case 1 and 3) and persistent oscillations (Case 2 and 4). This variation confirms that conventional GFM-based GCIs lack stability under large frequency drops. Conversely, TGFM limits peak overshoot to 2.4 W and

achieves full recovery within 1 s, validating its tight grid-forming capability across grid strengths.

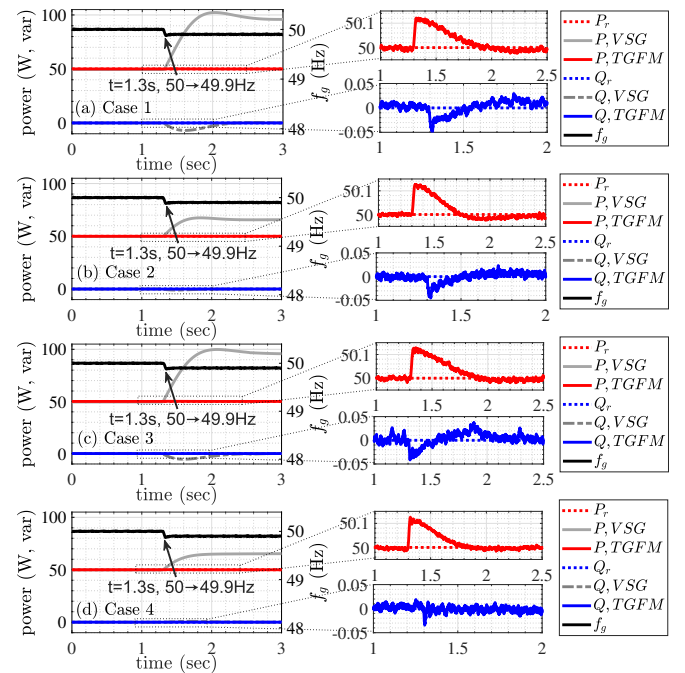


Fig. 21. Experimental waveforms of VSG and TGFM with different line impedances under 0.1 Hz frequency drops.

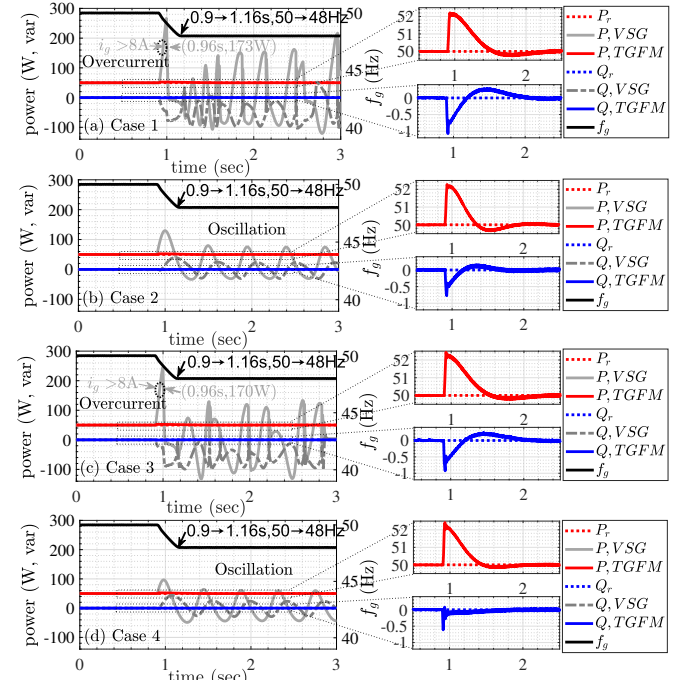


Fig. 22. Experimental waveforms of VSG and TGFM with different line impedances under 2 Hz frequency drops.

To further validate the proposed GFM control under diverse operating conditions, a different experimental setup (200 V DC-link, 40 V_{rms} grid voltage, 500 W), with other parameters unchanged, is implemented in the subsequent subsections.

B. Voltage Support by Dispatchable Power

This subsection experimentally validates the active and precise power support of TGFM strategy during several grid

frequency drops. As shown in Fig. 23 (a), the estimated frequency \hat{f}_g (red dashed) accurately tracks f_g (black solid). Using $P-f$ droop with gain K_{Pf} , the updated reference becomes $P_{r,\text{new}} = P^* + K_{Pf}(f_{g0} - \hat{f}_g)$. Thus, Fig. 23 (b) shows dynamic power response to frequency drops.

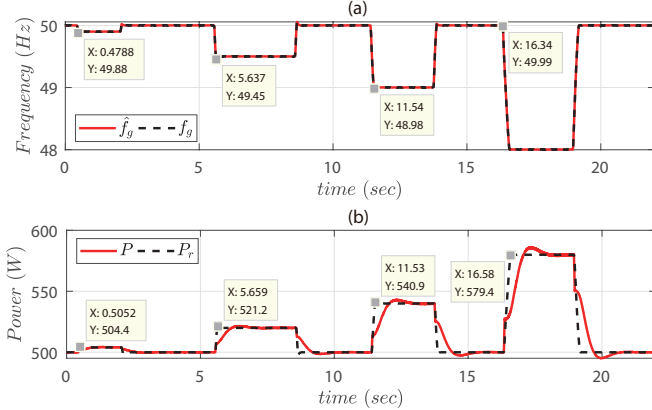


Fig. 23. Experimental waveforms of TGFM with Case 1 under different frequency drops.

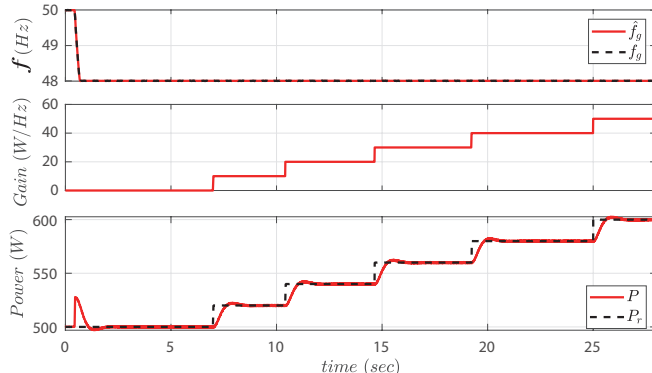


Fig. 24. Experimental waveforms of TGFM with Case 1 with different K_{Pf} gains.

Furthermore, as shown in Fig. 24, during a 2 Hz frequency drop, P_r is 500, 520, 540, 560, 580, and 600 W for $K_{Pf} = 0, 10, 20, 30, 40, 50$ W/Hz, respectively. This confirms that support power P_f is set by K_{Pf} . Precise power tracking and dispatchable targets enable GCIs to deliver active support while fully utilizing overcurrent margin, even during large frequency drops.

C. Parameter Robustness

In the above experiments, the L_g and R_g parameters employed by the observer were obtained from TABLE V. However, the acquisition of line impedance in real-world scenarios may introduce deviations. Therefore, the parameter robustness of the proposed method is evaluated in this subsection. Case 1 applies -50% mismatch in L_g and R_g (Fig. 25). This range is reasonable and sufficient [38], covering worst-case errors with margin.

As shown in Fig. 25 (a), a -50% reduction in L_g and R_g causes a slight rise in estimated frequency \hat{f}_g , which recovers to 50 Hz within 1 s. Fig. 25 (b) shows that the phase estimation error $\Delta\phi_g$ decreases and stabilizes within 1 s. Following a 2 Hz frequency drop at $t = 4$ s, active power exhibits a 20

W overshoot before settling at 500 W in 0.5 s. Subsequent parameter restoration to nominal ($t = 6.5$ s) and -50% ($t = 9.5$ s) confirms robust TGFM performance under large impedance mismatch and severe frequency disturbances.

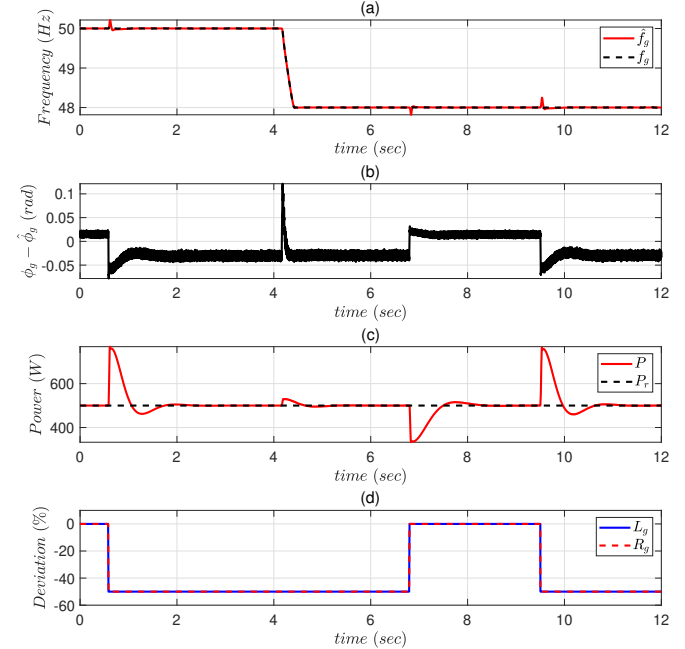


Fig. 25. Case 1: Phase angle estimation error and power deviation under a 2 Hz frequency drop with -50% impedance mismatch.

VI. CONCLUSION

This paper proposes a tight grid-forming (GFM) control framework to ensure inverter stability and reliable power delivery during large grid frequency drops across a wide range of SCR and X/R conditions. By integrating a grid voltage state observer, the proposed strategy actively compensates for grid phase deviations. This enables a paradigm shift from the passive and unpredictable P-delta response of conventional GFM to an active, dispatchable power control strategy that satisfies precise power dispatch requirements. This approach not only allows for proactive overcurrent management but also effectively prevents power instability, all while retaining the essential voltage-source characteristic of grid-forming control. Extensive simulations and rigorous proofs validate the method's effectiveness and superiority over existing GFM. The framework provides a novel operational paradigm for GCIs, offering an alternative to conventional approaches for navigating large frequency drops in future complex grids with high penetration of renewables and power electronics.

REFERENCES

- [1] Y. Gu and T. C. Green, "Power system stability with a high penetration of inverter-based resources," *Proceedings of the IEEE*, vol. 111, no. 7, pp. 832–853, 2023.
- [2] P. Lin, Q. Meng, M. Zhu, A. M. Y. M. Ghias, and F. Blaabjerg, "Dynamic circuit-based unified power regulation for hybrid ac/dc/ds microgrids: A comprehensive approach to static and transient control," *IEEE Transactions on Industrial Electronics*, pp. 1–12, 2025.
- [3] P. Lin, L. Du, H. Zhang, M. Zhu, J. Ma, and P. Wang, "Power lever: To transform interlinking architecture in hybrid ac/dc microgrids community," *IEEE Transactions on Industrial Electronics*, 2025.

- [4] B. Kroposki, "Achieving a 100% renewable grid: Operating electric power systems with extremely high levels of variable renewable energy," *IEEE Power and Energy Magazine*, vol. 15, no. 2, pp. 61–73, 2017.
- [5] NREC, "Grid forming functional specifications for bps-connected battery energy storage systems," North American Electric Reliability Corporation (NERC), Tech. Rep., June 2023, atlanta, GA, USA. [Online]. Available: https://www.nerc.com/comm/RSTC_Reliability_Guidelines/White_Paper_GFM_Functional_Specification.pdf
- [6] N. Hatzigyriou, J. Milanovic, C. Rahmann, V. Ajjarapu, C. Canizares, I. Erlich, D. Hill, I. Hiskens, I. Kamwa, B. Pal, P. Pourbeik, J. Sanchez-Gasca, A. Stankovic, T. Van Cutsem, V. Vittal, and C. Vournas, "Definition and classification of power system stability – revisited extended," *IEEE Transactions on Power Systems*, vol. 36, no. 4, pp. 3271–3281, 2021.
- [7] P. S. Kundur and O. P. Malik, *Power System Stability and Control*. New York City, NY, USA : McGraw-Hill Educ., 2022.
- [8] T. Xu, S. Jiang, Y. Zhu, and G. Konstantinou, "Composite power-frequency synchronization loop for enhanced frequency response considering current and power limits of grid-forming converters," *IEEE Transactions on Power Electronics*, vol. 40, no. 4, pp. 4969–4983, 2025.
- [9] C. MacIver, K. Bell, and M. Nedd, "An analysis of the august 9th 2019 gb transmission system frequency incident," *Electric Power Systems Research*, vol. 199, p. 107444, 2021. [Online]. Available: <https://www.sciencedirect.com/science/article/pii/S0378779621004259>
- [10] E. M. para la Transición Ecológica y el Reto Demográfico, "Versión no confidencial del informe del comité para el análisis de las circunstancias que concurrieron en la crisis de electricidad del 28 de abril de 2025," Tech. Rep., June 2025. [Online]. Available: <https://elmegavatio.com/energia/2025/el-miteco-presenta-el-informe-sobre-el-apagon-del-28-de-abril-de-2025>
- [11] B. Mahamed, M. Eskandari, J. E. Fletcher, and J. Zhu, "Sequence-based control strategy with current limiting for the fault ride-through of inverter-interfaced distributed generators," *IEEE Transactions on Sustainable Energy*, vol. 11, no. 1, pp. 165–174, 2020.
- [12] A. Moawwad, M. S. El Moursi, and W. Xiao, "A novel transient control strategy for vsc-hvdc connecting offshore wind power plant," *IEEE Transactions on Sustainable Energy*, vol. 5, no. 4, pp. 1056–1069, 2014.
- [13] N. Baeckeland, D. Venkatraman, M. Kleemann, and S. Dhople, "Stationary-frame grid-forming inverter control architectures for unbalanced fault-current limiting," *IEEE Transactions on Energy Conversion*, vol. 37, no. 4, pp. 2813–2825, 2022.
- [14] W. Du, Q. Nguyen, Y. Liu, and S. M. Mohiuddin, "A current limiting control strategy for single-loop droop-controlled grid-forming inverters under balanced and unbalanced faults," in *IEEE Energy Conversion Congress and Exposition (ECCE)*, 2022, pp. 1–7.
- [15] M. G. Taul, X. Wang, P. Davari, and F. Blaabjerg, "Current limiting control with enhanced dynamics of grid-forming converters during fault conditions," *IEEE Journal of Emerging and Selected Topics in Power Electronics*, vol. 8, no. 2, pp. 1062–1073, 2020.
- [16] T. Liu, X. Wang, F. Liu, K. Xin, and Y. Liu, "A current limiting method for single-loop voltage-magnitude controlled grid-forming converters during symmetrical faults," *IEEE Transactions on Power Electronics*, vol. 37, no. 4, pp. 4751–4763, 2022.
- [17] X. Lu, J. Wang, J. M. Guerrero, and D. Zhao, "Virtual-impedance-based fault current limiters for inverted dominated ac microgrids," *IEEE Transactions on Smart Grid*, vol. 9, no. 3, pp. 1599–1612, 2018.
- [18] Z. Shuai, W. Huang, C. Shen, J. Ge, and Z. J. Shen, "Characteristics and restraining method of fast transient inrush fault currents in synchronverters," *IEEE Transactions on Industrial Electronics*, vol. 64, no. 9, pp. 7487–7497, 2017.
- [19] F. Han, X. Zhang, M. Li, F. Li, and W. Zhao, "Stability control for grid-connected inverters based on hybrid-mode of grid-following and grid-forming," *IEEE Transactions on Industrial Electronics*, vol. 71, no. 9, pp. 10 750–10 760, 2024.
- [20] P. Wang, J. Ma, R. Zhang, S. Wang, T. Liu, Z. Wu, and R. Wang, "Power self-synchronization control of grid-forming voltage-source converters against a wide range of short-circuit ratio," *IEEE Transactions on Power Electronics*, vol. 38, no. 12, pp. 15 419–15 432, 2023.
- [21] F. Zhao, X. Wang, Z. Zhou, Y. Sun, L. Harnefors, and T. Zhu, "Robust grid-forming control with active susceptance," *IEEE Transactions on Power Electronics*, vol. 38, no. 3, pp. 2872–2877, 2023.
- [22] L. Huang, C. Wu, D. Zhou, and F. Blaabjerg, "A power-angle-based adaptive overcurrent protection scheme for grid-forming inverter under large grid disturbances," *IEEE Transactions on Industrial Electronics*, vol. 70, no. 6, pp. 5927–5936, 2023.
- [23] N. Mohammed, M. H. Ravanji, W. Zhou, and B. Bahrani, "Online grid impedance estimation-based adaptive control of virtual synchronous gen-
- erators considering strong and weak grid conditions," *IEEE Transactions on Sustainable Energy*, vol. 14, no. 1, pp. 673–687, 2023.
- [24] Y. Qu, F. Bai, and R. Yan, "Adaptive controller based on stability boundaries for grid-forming and grid-following inverters under varying grid impedance," *IEEE Transactions on Sustainable Energy*, pp. 1–14, 2025.
- [25] B. Shao, Q. Xiao, L. Xiong, L. Wang, Y. Yang, Z. Chen, F. Blaabjerg, and J. M. Guerrero, "Power coupling analysis and improved decoupling control for the vsc connected to a weak ac grid," *International Journal of Electrical Power & Energy Systems*, vol. 145, p. 108645, 2023.
- [26] T. Wen, D. Zhu, X. Zou, B. Jiang, L. Peng, and Y. Kang, "Power coupling mechanism analysis and improved decoupling control for virtual synchronous generator," *IEEE Transactions on Power Electronics*, vol. 36, no. 3, pp. 3028–3041, 2021.
- [27] S. Coffey, S. Harrison, A. Egea-Alvarez, and C. Brozio, "Limitations and comparisons of small signal modelling techniques in converter dominated medium voltage networks," in *2023 25th European Conference on Power Electronics and Applications (EPE'23 ECCE Europe)*, 2023, pp. 1–8.
- [28] R. Yin, Y. Sun, S. Wang, and L. Zhang, "Stability analysis of the grid-tied vsc considering the influence of short circuit ratio and x/r ," *IEEE Transactions on Circuits and Systems II: Express Briefs*, vol. 69, no. 1, pp. 129–133, 2022.
- [29] N. G. ESO, "Great britain grid forming best practice guide," Tech. Rep., Apr 2023. [Online]. Available: <https://www.nationalgrideso.com/document/278491/download>
- [30] H. Wu, X. Wang, and L. Zhao, "Design considerations of current-limiting control for grid-forming capability enhancement of vscs under large grid disturbances," *IEEE Transactions on Power Electronics*, vol. 39, no. 10, pp. 12 081–12 085, 2024.
- [31] K. V. Kkuni and G. Yang, "Effects of current limit for grid forming converters on transient stability: analysis and solution," *International Journal of Electrical Power & Energy Systems*, vol. 158, p. 109919, 2024.
- [32] X. Niu, C. Zhang, Y. Qu, X. Wang, and H. Li, "A new composite control strategy for large-signal stabilization of constant power loads in islanded ac microgrids," *IEEE Transactions on Smart Grid*, vol. 15, no. 5, pp. 4407–4423, 2024.
- [33] X. Niu, C. Zhang, and C. Cui, "Composite dynamic regulation for ac microgrids feeding variable constant power loads," in *2024 IEEE 19th Conference on Industrial Electronics and Applications (ICIEA)*, 2024, pp. 1–6.
- [34] C. Zhang, M. Li, L. Zhou, C. Cui, and L. Xu, "A variable self-tuning horizon mechanism for generalized dynamic predictive control on dc/dc boost converters feeding cpl," *IEEE Journal of Emerging and Selected Topics in Power Electronics*, vol. 11, no. 2, pp. 1650–1660, 2023.
- [35] X. Wang, X. Dong, X. Niu, C. Zhang, C. Cui, J. Huang, and P. Lin, "Toward balancing dynamic performance and system stability for dc microgrids: A new decentralized adaptive control strategy," *IEEE Transactions on Smart Grid*, vol. 13, no. 5, pp. 3439–3451, 2022.
- [36] N. Baeckeland, D. Chatterjee, M. Lu, B. Johnson, and G.-S. Seo, "Overcurrent limiting in grid-forming inverters: A comprehensive review and discussion," *IEEE Transactions on Power Electronics*, vol. 39, no. 11, pp. 14 493–14 517, 2024.
- [37] W. Chen, "Disturbance observer based control for nonlinear systems," *IEEE/ASME Transactions on Mechatronics*, vol. 9, no. 4, p. 706–710, 2004.
- [38] N. Mohammed, M. Ciobotaru, and G. Town, "Fundamental grid impedance estimation using grid-connected inverters: a comparison of two frequency-based estimation techniques," *IET Power Electronics*, vol. 13, no. 13, pp. 2730–2741, 2020.



Xitong Niu (Student Member, IEEE) received the M.Sc degree in electrical engineering from Shanghai University of Electric Power, China, in 2018. He was with Unitech Embedded and KUKA Company from 2018 to 2023, focusing on power electronic systems. He is currently working toward the Ph.D. degree in electrical engineering from the School of Electrical Engineering, Shanghai University of Electric Power, Shanghai, China. He is currently a Visiting Ph.D. Student with the Department of Electrical and Computer Engineering, National University of Singapore, Singapore, Singapore. His research interests include advanced algorithm in power electronic systems and microgrids.



Mrutyunjaya Sahani (Senior Research Fellow, IEEE) received the B.Tech. degree in electrical engineering from the Biju Patnaik University of Technology, Rourkela, India, in 2007, the M.Tech. degree in embedded system technology from the SRM University, Chennai, India, in 2010, and the Ph.D. degree in electronics and communication engineering from Siksha 'O' Anusandhan University, Odisha, India, in 2019. He is currently a Research Fellow with the Department of Electrical and Computer Engineering, National University of Singapore, Singapore. His current research interests include power quality analysis, power system protection, signal processing, micro and smart grid, renewable energy integration, energy management, artificial intelligence, and embedded system design.



Yue Qu (Student Member, IEEE) received her M.Eng. degree in Control Engineering from Shanghai University of Electric Power, China, in 2020. She is currently working toward her Ph.D. degree in Electrical and Electronic Engineering at Griffith University and the University of Queensland, Australia. Her research interests include the control of power electronics systems and the grid integration of renewable energy resources.



Chuanlin Zhang (Senior Member, IEEE) received the B.S. degree in mathematics and the Ph.D. degree in control theory and control engineering from the School of Automation, Southeast University, Nanjing, China, in 2008 and 2014, respectively. He was a Visiting Ph.D. Student with the Department of Electrical and Computer Engineering, University of Texas at San Antonio, San Antonio, TX, USA, from 2011 to 2012, and a Visiting Scholar with the Energy Research Institute, Nanyang Technological University, Singapore, from 2016 to 2017. Since 2014, he has been with the College of Automation Engineering, Shanghai University of Electric Power, Shanghai, China, where he is currently a Professor. His current research interests include nonlinear system control theory and applications for power systems.



Shanghai Jiao Tong University. His research interests include power system stability / reliability analyses, smart grid cyber-physical security, and artificial intelligence analytics.



Sanjib Kumar Panda (Fellow, IEEE) received the B.Eng. degree from the South Gujarat University, Surat, India, in 1983, the M.Tech. degree from the Indian Institute of Technology, Banaras Hindu University, Varanasi, India, in 1987, and the Ph.D. degree from the University of Cambridge, Cambridge, U.K., in 1991, all in electrical engineering. Since 1992, he has been holding a faculty position with the Department of Electrical and Computer Engineering, National University of Singapore, Singapore, where he is currently an Associate Professor and the Director of the Power & Energy Research Area. He has authored or coauthored more than 450 peer-reviewed research papers, coauthored one book, and contributed to several book chapters. He holds ten patents, and is the co-founder of three start-up companies. His research interests include high-performance control of motor drives and power electronic converters, condition monitoring and predictive maintenance, and building energy efficiency enhancement. He is an Associate Editor for IEEE Transactions on Power Electronics, IEEE Transactions on Industry Applications, IEEE Transactions on Energy Conversion, IEEE Access, and IEEE Journal of Emerging and Selected Topics in Power Electronics. He is an IEEE PELS Distinguished Lecture for 2022–2023. He is the Chair of the IEEE PELS Technical Committee, TC-12: Energy Access and Off-grid Systems. Since 2016, he has also been the R-10 Membership & Chapter Development Coordinator for IEEE PELS since 2016. Dr. Panda was the recipient of the Cambridge-Nehru Scholarship and the M. T. Mayer Graduate Scholarship during his Ph.D. study (1987–1991).



Chengang Cui (Member, IEEE) received the B.E. degree in automation engineering from Jilin University, Changchun, China, in 2004, and the Ph.D. degree in control theory and control from Zhejiang University, Hangzhou, China, in 2010. Since 2015, he has been with the College of Automation Engineering, Shanghai University of Electric Power, Shanghai, China, where he is currently an Associate Professor. He worked with Shanghai Institute for Advanced Studies, Chinese Academy of Sciences, Shanghai, China, engaged in energy management and optimal scheduling from 2012 to 2015. His research interests include the control and schedule of renewable energy systems and microgrid.